Temporal manipulation of period-2 polarization domain wall solitons in a nonlinear fiber Kerr resonator

Julien Fatome, Nicolas Berti, Bertrand Kibler, Gang Xu, Stuart Murdoch, Miro Erkintalo, Stéphane Coen

Temporal manipulation of period-2 polarization domain wall solitons in a nonlinear fiber Kerr resonator

JULIEN FATOME[1,2*], NICOLAS BERTI[1], BERTRAND KIBLER[1]
GANG XU[2], STUART G. MURDOCH[2], MIRO ERKINTALO[2] AND STEPHANE COEN[2]

[1]*Laboratoire Interdisciplinaire Carnot de Bourgogne, UMR 6303 CNRS Université de Bourgogne, Dijon, France*
[2]*The University of Auckland, Private Bag 92019, Auckland 1142, New Zealand*

**Corresponding author: Julien.Fatome@u-bourgogne.fr*

We report on the experimental demonstration of temporal manipulations of dissipative polarization domain wall solitons in a Kerr nonlinear resonator operated in a period-doubled configuration. Our experiments are performed in a coherently driven normally dispersive fiber ring cavity, in which polarization domains emerge in virtue of a spontaneous symmetry breaking phenomenon. The addition of a lumped birefringent defect into the cavity forces their polarization components to swap on a two-round-trip cycle, thus protecting them from the deleterious impact of the system's asymmetries. We exploit these symbiotic dynamics in proof-of-concept buffering experiments, in which these dissipative structures are addressed individually and temporally manipulated through phase-encoded perturbations imprinted onto the driving beam. Our results provide new insights into the practical exploitation of spontaneous symmetry breaking mechanisms and the use of two-component dissipative structures for all-optical data storage applications.

1. Introduction

Domain walls (DWs) are kink-type topological structures that connect two homogeneous stable states of a physical system. They are known to occur as a result of a phase transition or spontaneous symmetry breaking mechanisms (SSB) and have been observed in numerous fields of science including ferromagnetism [1-5], Bose-Einstein condensates [6-7], hydrodynamics [8] and nonlinear optics [9]. In the latter, DWs mostly rely on the vectorial nature of light and hence, are known as polarization domain walls (PDWs) [10-12]. They correspond to interlaced kink-solitons able to self-propagate in the defocusing regime of a two-component waveguide and are fundamentally related to the polarization modulation instability phenomenon occurring in isotropic optical fibers [13-15]. In close analogy with DWs encountered in ferromagnetic materials, these *polarization knots* segregate adjacent parts of the field into homogeneous domains of opposite handedness. The robustness of these structures has been exploited for the transmission of topological data in strongly defocusing regimes of optical fibers [16]. On the other hand, PDWs can also exist in dissipative optical systems. Whereas antiphase switching behaviors at nanosecond scales have been reported in fiber lasers through cross-saturation dynamics [17-19] and in vertical-cavity surface-emitting lasers [20], dissipative PDW solitons have been recently observed for the first time in a coherently driven fiber Kerr resonator [21-22]. Their existence relies on the polarization SSB of the intra-cavity field, segregating two hybrid modes of opposite handedness by the virtue of the nonreciprocity imposed by their cross-phase modulation (XPM) coupling [23-28]. This bifurcation process can be explained as a self-amplification of small power fluctuations taking place between these two, degenerate, and incoherently coupled eigenmodes [28-29]. Recently, we have also shown that the inclusion into the resonator of a π-phase shift birefringent defect provides a topological protection of SSB against unwanted system asymmetries [30]. More precisely, the presence of a localized birefringent defect makes the light's handedness to swap at every cavity round-trip, giving rise to a fast polarization flip-flopping on a two-round-trip cycle (P2). This precessing motion leads to a self-symmetrization of the dynamics, thus conferring to these P2-PDW solitons an unprecedented robustness, whilst enabling the realization of SSB in effective ideal conditions [30].

In this new contribution, inspired by previous works reporting temporal manipulations of bright cavity solitons (CSs) in coherently-driven fiber Kerr resonators [31-36], we demonstrate that these dissipative P2-PDWs can be exploited as topological bits and are able to persist indefinitely in a fiber ring cavity. Furthermore, we also show that their temporal location can be trapped and dynamically controlled thanks to a shallow phase modulation imprinted on the coherent driving beam. Our results provide new insights into the exploitation of vectorial dissipative solitons in defocusing Kerr resonators as robust bit-entities for all-optical data storage applications and more generally, pave the way to new opportunities for the implementation of robust spontaneous symmetry breaking phenomena in practical systems.

2. Experimental setup

Our experimental setup is depicted in Fig. 1(a) and is rather similar that described in Ref. [30]. The passive Kerr resonator consists of a normally dispersive fiber ring cavity made of a $L = 12$-m long segment of spun — nearly isotropic — optical fiber. The second-order dispersion is estimated to $\beta_2 = 47\ \mathrm{ps^2\,km^{-1}}$ at the pump wavelength, and the nonlinear Kerr coefficient is $\gamma = 4\ \mathrm{W^{-1}km^{-1}}$. Note that the defocusing (normal dispersion) regime is here a prerequisite to the formation of PDWs and mandatory to avoid the breakup of the circulating field due to usual scalar modulational instability [37-38]. Our fiber cavity presents a free spectral range (FSR) of 17.54 MHz and a finesse near 27 — the finesse is mainly limited by the splicing and the difference of core size between the spun fiber (5 µm) and the input coupler (10 µm). The resonator is coherently-driven by means of a 1552.4-nm cw-laser (linewidth <1 kHz), whose central frequency can be locked at a fixed absolute detuning from a resonance thanks to a proportional-integral-derivative (PID) feedback loop. The cw-laser is intensity-modulated to generate 1.1-ns square pulses [see Fig. 1(b)], whose repetition rate is carefully adjusted to match the FSR of the cavity. A phase modulation scheme is also implemented on the driving field to enable both excitation and temporal manipulation of P2-PDWs. Indeed, it is well known for bright CSs that the application of a phase modulation on top of the circulating pulses provides a change of instantaneous frequency, which in turn by virtue of group velocity dispersion, enables retiming functionalities through a temporal drift proportional to $-\beta_2 L\phi'(\tau)$, where $\phi(\tau)$ corresponds to the phase modulation of the driving beam along the fast-time coordinate τ [31-33, 39-41]. Similarly, in our normally dispersive cavity, the PDWs circulating along the leading edge of the phase profile will experience a negative delay, whereas they will experience a positive drift on the trailing edge. Consequently, the PDWs will be attracted to the nearest minima of the phase profile, which therefore corresponds to a stable trapping site. To demonstrate such capabilities with P2-PDWs, a 10-GHz shallow phase modulation was imprinted to the driving field so as to trap the PDWs onto a 10-Gbit/s temporal reference grid. Additionally, an electrical phase shifter, driven by an arbitrary waveform generator (AWG), allows us to dynamically modify the temporal location of these P2-PDWs. Furthermore, engineered phase perturbations were generated on demand thanks to a pulse pattern generator (PPG) to trigger the emergence of PDW solitons into the cavity. The resulting driving pulse train is then amplified by means of an Erbium-doped fiber amplifier (EDFA) before optical filtering and injection into the resonator. At each round-trip, the driving field is superimposed on the circulating signal through a 90:10 fiber coupler. A 1% tap-coupler is also inserted inside the resonator to extract a portion of the intra-cavity field for polarization and temporal diagnostic measurements.

Polarization control of the present setup is quite sensitive and requires no less than three polarization controllers (PCs). First-of-all, the polarization of the driving field is carefully adjusted at the input of the resonator through PC1 so as to predominately excite one of the principal polarization modes of the cavity E_x — defined as polarization modes that return to their original polarization after one round-trip. Next, a second polarization controller (PC2) is mounted directly onto a short portion of the fiber cavity to introduce a phase birefringent defect through local mechanical stress. This amount of extra phase-shift is finely adjusted in such a way to offset the phase shift of the second orthogonal principal mode E_y by π. Note that this quantity can be precisely tuned by monitoring the cavity resonances while scanning the laser frequency [see Fig. 1(c)]. This localized defect acts as an intra-cavity half-wave plate, inverting the sign of the y-component at each round-trip $E_y \longrightarrow E_y e^{i\pi} = -E_y$, hence forcing the light's handedness to swap and conferring to PDWs the desired flip-flopping period-2 dynamics [30]. Finally, at the output of the resonator, a third polarization controller (PC3), associated with a polarizing-beam-splitter (PBS), is used to project the intra-cavity field into different polarization basis of interest i.e., along the two principal modes of the cavity and along two, degenerate, hybrid eigenmodes of opposite handedness defined as $E_\pm = (E_x \pm iE_y)/\sqrt{2}$. These output signals are finally characterized in the temporal domain by means of ultra-fast photodetectors connected to an 80-GSa/s, 50-GHz bandwidth real-time oscilloscope or a 70-GHz bandwidth sampling oscilloscope.

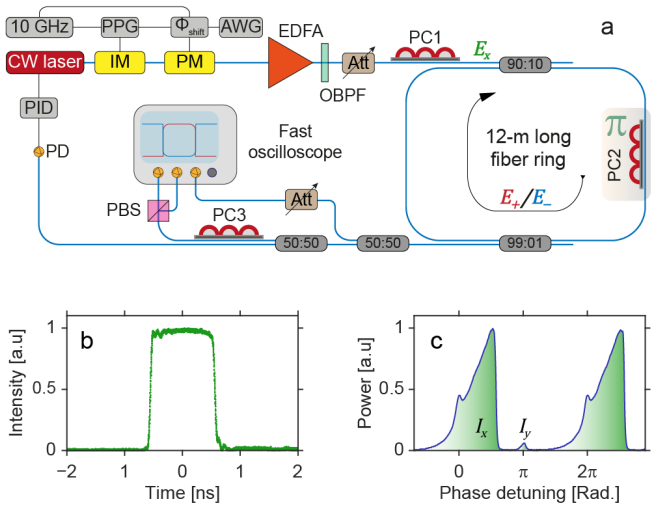

Fig. 1. (a) Experimental setup. PPG: pulse pattern generator, IM: intensity modulator, PM: phase modulator, ϕ_{shift}: electrical phase shifter, AWG: arbitrary waveform generator, PC: polarization controller, EDFA: Erbium doped fiber amplifier, OBPF: optical bandpass filter, Att: variable attenuator, PBS: polarization beam splitter, PID: proportional integral derivative system, PD: photodetector. (b) Input pulse profile. (c) Nonlinear resonances of the cavity measured for a driving power of 11 W.

3. Modelling

To model our experiments, we take advantage of a vectorial Ikeda map approach, which can accurately account for both the cavity boundary conditions and the localized nature of the π-phase shift birefringent defect [21]. Note that a set of coupled Lugiato-Lefever equations derived on a two round-trip mean-field approach has been also shown to accurately model the present system, especially its self-induced symmetrization [30]. However, here we take advantage of the full map model so as to investigate the polarization swapping dynamics on each subsequent round-trip.

The evolution of both hybrid modes $E_\pm(t,\tau)$ of the electric field envelope along the m^{th} round-trip is governed by the following set

of two nonlinear Schrödinger equations, incoherently coupled through the Kerr-induced cross-phase modulation [42]:

$$\begin{cases} \left[i\frac{\partial E_{\pm}}{\partial z} = \frac{\beta_2}{2}\frac{\partial^2 E_{\pm}}{\partial \tau^2} - \gamma\left(|E_{\pm}|^2 + 2|E_{\mp}|^2\right)E_{\pm} \right]^{(m)} \\ \begin{pmatrix} E_+ \\ E_- \end{pmatrix}^{(m+1)} = e^{-\alpha}\begin{pmatrix} E_- \\ E_+ \end{pmatrix}^{(m)} e^{-i\delta_0} + \sqrt{\theta}S_{\text{in}}\begin{pmatrix} \cos(\pi/4+\delta_\chi) \\ \sin(\pi/4+\delta_\chi) \end{pmatrix} \end{cases}, (1)$$

in which, z represents the propagation distance within the cavity, m the round-trip index and τ the fast-time expressed in a delayed reference frame. These equations are then completed by boundary conditions to describe first, the coherent superposition of the intra-cavity field with the driving field at each round-trip, and second to take into account for the swapping process $E_{\pm} \rightleftharpoons E_{\mp}$ induced by the π-phase shift birefringent defect. θ represents the coupling coefficient of the input coupler, whilst α is half of the power loss per cavity round-trip ($\alpha = 0.116$). S_{in} stands for the driving field, while δ_χ represents its ellipticity offset (supposed to be small) with respect to perfect symmetric conditions $\pi/4$ i.e., how much the driving power is imbalanced between the two hybrid modes $E_{\pm}$. Finally, δ_0 is the phase detuning parameter of the driving field with respect to the nearest cavity resonance.

It is well known that by virtue of the nonreciprocity of the XPM term in Eqs. (1), this class of two-component dissipative system can undergo a polarization SSB of its scalar homogenous steady states (HSSs) in favor of two mirror-like asymmetric solutions of opposite ellipticity [23-25]. This behavior is illustrated in Fig. 2(a) in which we have reported the numerical evolution of the normalized Stokes parameters of the HSSs on two consecutive round-trips as a function of the cavity detuning and for a driving power corresponding to our experimental configuration $|S_{in}|^2$= 11 W. The Stokes parameters are classically defined as: $S_1 = 2Re(E_+E_-^*)$, $S_2 = -2Im(E_+E_-^*)$ and $S_3 = |E_+|^2 - |E_-|^2$. Under perfectly symmetrical conditions ($\delta_\chi = 0$) and moderate intra-cavity power, the degenerate eigenmodes with opposite handedness $E_{\pm}$ should have identical intensities i.e., the chirality of the system, defined as $\zeta = S_3/|S_3|$ should be close to zero. This classical behavior is well observed in Fig. 2(a) at low cavity detuning for which the system is ruled by the scalar dynamics where $S_1 = 1, S_{2,3} = 0$. However, for higher detuning i.e., δ_0~0.2 rad, the system exhibits vectorial behaviors. More specifically, the intensity of the two polarization components I_+ and I_- undergo a pitchfork bifurcation, characterized by two novel solutions of opposite ellipticity $\pm S_3$. Increasing further the cavity detuning unveils a strong chirality in the system dynamics with two mirror-like HSSs such that $S_3 \sim \pm 1$. Note that this kind of SSB phenomenon is often characterized as hidden symmetry, since the two asymmetric states are still mirror-symmetric with respect to each other, though only one can be eventually observed at each realization [43]. However, in our configuration, the P2 swapping dynamic allows us to uncloak this hidden symmetry, revealing both asymmetric states as well as the full bifurcation diagram on a two-round-trip cycle. The formation of dissipative P2-PDWs in our Kerr resonator is then sustained in-between these two flip-flopping solutions, for which sharp temporal transitions segregate the circulating field into well-separated domains of opposite ellipticity, as illustrated in Fig. 2(b).

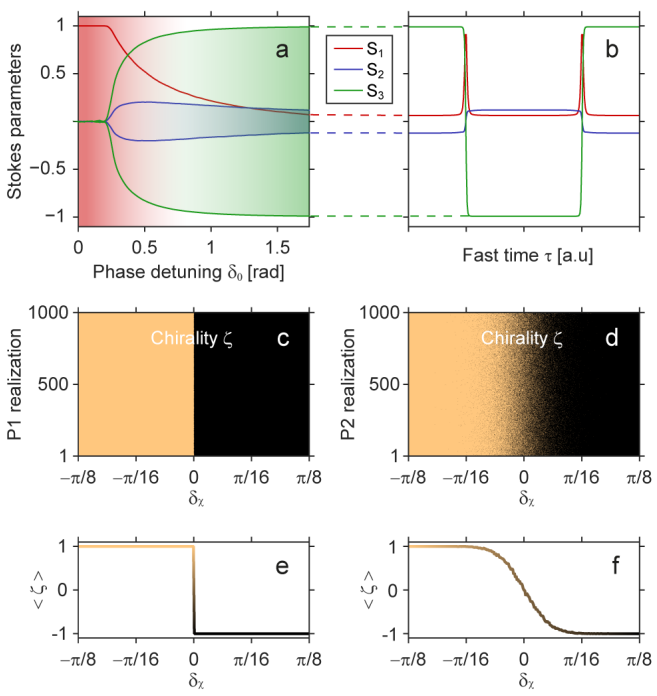

Fig. 2. (a) Numerical evolution of the Stokes parameters of the HSSs with respect to the phase detuning of the cavity and for a driving power of 11 W. (S_1 in red, S_2 in blue and S_3 in green). (b) Temporal profile of a P2-PDW soliton. (c-d) Chirality of the system emerging from the polarization SSB as a function of the driving field ellipticity and for 1000 different realizations. Ochre: $\zeta = +1$, black: $\zeta = -1$. (c) P1 configuration (without birefringent defect). (d) P2 configuration. (e-f) Corresponding average chirality with respect to the driving ellipticity.

The robustness of the P2-SSB configuration can be illustrated by measuring its lack of randomness and average chirality in presence of a slight ellipticity in the driving field ($\delta_\chi \neq 0$) i.e., an imbalance of pump power between both hybrid modes. This behavior is depicted in Figs. 2(c-d), in which we have reported for 1000 different numerical realizations, the chirality ζ emerging from the system after scanning the bifurcation diagram of Fig. 2(a), respectively without [P1, panel (c)] and with [P2, panel (d)] the inclusion of the π-phase shift birefringent defect. Panel (c) shows that the P1 configuration leads to a sharp transition in-between two areas, clearly highlighting the extreme sensitivity of the SSB phenomenon with respect to an initial bias in system's parameters. Consequently, the average chirality, represented in panel (e) and reflecting the probability of occurrence of both mirror-like solutions, arises as a sharp step-like transition. Indeed, the presence of an infinitesimal imbalance of driving power instantaneously favors one of the two mirror-like solutions, making practical implementations of P1-SSB quite challenging in a real-world *imperfect* environment.

In stark contrast, as shown in panel (d), the flipping dynamics associated to the P2 configuration leads to a smooth transition of occurrence between the two branches of the bifurcation diagram. In fact, both hybrid modes harvest alternatively a depression and a rise in their driving power, leading to an average value of $\sqrt{\theta/2}\,S_{\text{in}}\cos\delta_\chi$ on a two-round-trip cycle. Therefore, as can be observed in panel (f), this self-symmetrization process restores an

equal-probability in the occurrence of both mirror-like HSSs on a wide range of driving ellipticity, thus making the P2 configuration highly promising for practical applications based on polarization SSB.

4. Experimental generation of P2-PDWs

In the following experimental sections, the generation and manipulations of P2-PDWs in our fiber cavity are carried out for a constant detuning value of $\delta_0 = 1.16$ rad and a fixed driving peak power of 11 W. As already highlighted in Fig. 2(a), these system's parameters place our configuration above the threshold of pitch-fork bifurcation, thus providing a high level of contrast between the two HSS solutions $I_{\pm}$.

Figure 3 summarizes the typical recordings of P2-PDW solitons circulating around our fiber ring cavity. For these measurements, we first excite P2-PDWs through phase perturbations of the driving field so as to spontaneously create localized temporal transitions between the upper and lower branches of the HSS bifurcation diagram. This phase perturbation corresponds to a π-phase jump imposed on the driving beam over 100 round-trips and induces a transient regime from which a random pattern of PDWs is then created. Subsequently, the 10-GHz shallow phase modulation plays the role of a periodic potential [31-33], which allows us to trap and distribute the generated PDWs along a reference temporal grid, whilst overcoming the slight desynchronization of the driving pulses with respect to the cavity FSR, thus extending the long-term stability of PDWs.

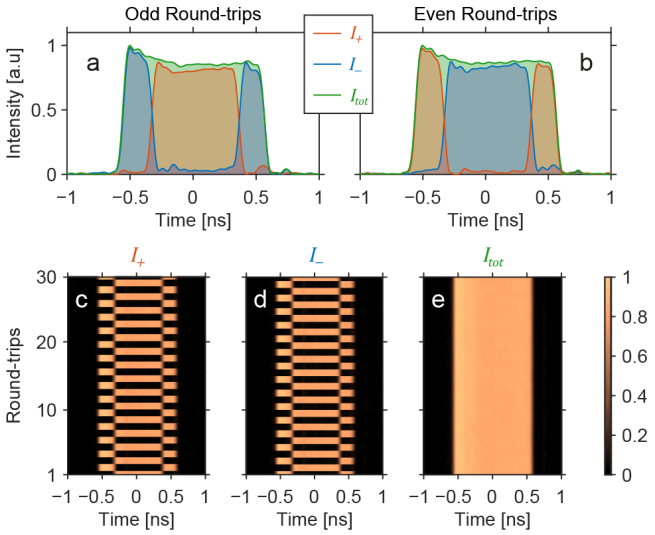

Fig. 3. (a-b) Temporal profiles of P2-PDW solitons recorded on two consecutive round-trips for $\delta_0 = 1.16$ rad and a driving peak power of 11 W. The two polarization components I_+ and I_- are reported in red and blue, respectively. The total intensity is depicted in green. (c-e) Pseudo-color plots showing the real-time evolution of the P2-PDWs pattern along 30 consecutive round-trips; from left to right: I_+ component, I_- and total intensity.

Figures 3(a-b) depicts the intensity profiles of the P2-PDW pattern monitored in the $E_{\pm}$ basis over two consecutive round-trips. First-of-all, we can observe that the two polarization components exhibit an anti-correlated temporal behavior, splitting the circulating ns-pulse into adjacent domains of opposite ellipticity. Next, we can further notice that both polarization components swap their temporal profiles from one round-trip to the next, hence unveiling the period-2 flipping dynamic imposed by the intra-cavity π-phase-shift defect. Finally, the total intensity, also reported in panels (a-b) with green solid-lines, remains nearly constant, confirming the vectorial nature of this pattern.

The spinning motion of these temporal structures is even more striking when reporting the real-time evolution of both polarization components with respect to round-trip index. Indeed, the resulting spatio-temporal diagrams, displayed in Figs. 3(c-d), exhibit a perfectly anti-correlated woven structure, confirming the presence of stable PDW solitons in our fiber cavity. Moreover, the flip-flopping motion is readably observable as both anti-correlated patterns swap at every cavity round-trip. Remarkably, the total intensity, shown in panel (e), remains perfectly preserved during the whole propagation, further confirming the polarization nature of these structures and their underlying swapping dynamics.

5. Phase constellations of P2-PDWs

Since P2-PDWs are in essence flip-flopping phase kink-solitons, the swapping dynamics highlighted above can be deeper characterized by performing a homodyne coherent detection of the circulating field. To this aim, two PDWs are first excited into the ring cavity, whilst their polarization components $E_{x/y}$ are demultiplexed thanks to the output PBS and mixed within an 90° hybrid coupler associated to two balanced detectors. Each detector then provides a direct monitoring of the in-phase $I = 4Re\left(E_x E_y^*\right)$ and quadrature $Q = 4Im\left(E_x E_y^*\right)$ components of the intra-cavity field, respectively [44]. Figure 4(a) illustrates a typical temporal trace of the I/Q components of the PDW pattern and clearly emphasizes the kink-nature of the PDW solitons with two adjacent domains of opposite phase.

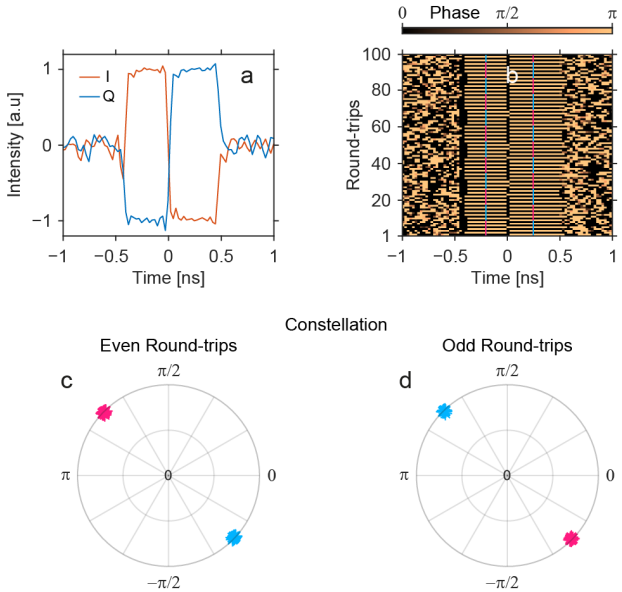

Fig. 4. (a) Typical experimental I/Q coherent detection of P2-PDWs. (b) Pseudo-color plots showing the real-time evolution of the P2-PDWs phase pattern along 100 consecutive round-trips. (c-d) Phase constellations

recorded along the Even (c) and Odd (d) round-trips. The magenta and cyan spots indicate the phase evaluated along two different fast-time location corresponding to both color dash-lines of panel b. These diagrams clearly reveal the phase nature of PDW solitons as well as the π-phase shift induced polarization swapping on every cavity round-trip.

From these measurements, we have next extracted the phase of these temporal structures along consecutive round-trips and reported its evolution in Fig. 4(b). The resulting spatio-temporal diagram first confirms the kink-nature of these localized polarization entities and further reveals the phase swapping effect imposed by the lumped birefringent defect on every cavity round-trip. This phase dynamics is even more readable when plotting the phase constellation corresponding to Even (Panel c) and Odd (panel d) round-trips for the two PDWs under-analysis. The diametrically opposite positions of the two cyan and magenta spots in the complex plane demonstrates that the relative phase in-between the *x* and *y* components are in quadrature for each polarization domain and is flipped by π at each cavity round-trip.

6. Long-term stability of P2-PDWs

To assess the robustness of the P2-PDW entities against fluctuations and asymmetries, we have performed a long-term measurement of their temporal and polarization properties over a very large number of round-trips. To this aim, we excite a single P2-PDW in the cavity that splits the intra-cavity field in two well-defined regions of orthogonal polarizations. Figure 5(a) displays the concatenation of the intensity profiles recorded for each polarization component I_+ and I_- as a function of the cumulative distance run through the resonator. Note that for sake of clarity, only odd round-trips are represented to conceal the polarization swapping effect. As can be seen, these P2-PDWs reveal an extreme longevity, especially when compared to the first observation of dissipative PDWs reported in ref. [22]. Indeed, while this earlier observation of dissipative PDWs has been performed on a 30s laboratory timescale, here the self-symmetrized P2-PDWs are able to persist in our resonator for more than 30 minutes (mainly limited by the long-term thermal drift of the cavity). This 30-minute duration represents an equivalent transmission of more than twice the Earth-Sun distance, evidencing a major step of improvement for practical applications.

In addition, we have depicted in Fig. 5(b) a temporal zoom on the transition area of the P2-PDW separating the two domains of polarization. The rise-time is found to be 13 ps, which is mainly due to the limited bandwidth of our detection setup (70 GHz). Nevertheless, it has been found in good agreement with numerical predictions, when these latter are convoluted with the photodetector's response (open circles). Additionally, Fig. 5(c) displays the corresponding experimental optical spectrum as a green solid line, and is compared with the numerical predictions (in purple). Despite a slight asymmetry in the experimental spectrum, attributed to the pump profile and weak desynchronization of the ns-driving pulses, the agreement still appears very good. We can also notice the presence of small bumps localized on both edges of the spectrum, characteristic of the shock front dynamics of the pumped pulse in defocusing regime [45].

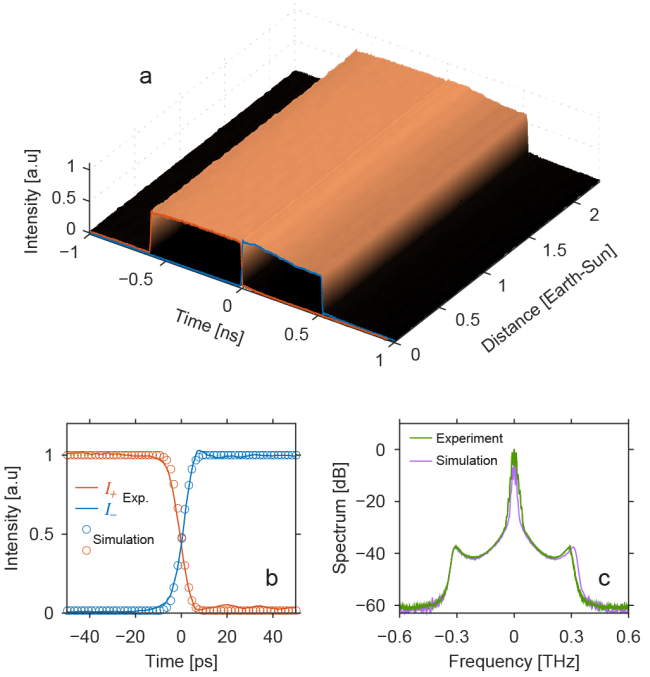

Fig. 5. (a) Space-time-intensity diagram showing the experimental evolution of both intra-cavity polarization components $I_\pm$ of a single P2-PDW soliton as a function of propagation distance run in the resonator and expressed in equivalent of Earth-Sun distances (149.6 M of kms). Note that only odd-roundtrips are represented for clearness purpose. As in previous results, $\delta_0 = 1.16$ rad and the driving power is 11 W. Temporal traces of I_+ and I_- at first round-trip are also depicted with red and blue solid lines, respectively. (b) Experimental temporal profile of the kink-transition between the two polarization domains recorded thanks to a 70-GHz bandwidth photodetector (solid lines). Numerical predictions of Eqs. (1) are also indicated with circles after convolution with the photodetector's frequency response. (c) Experimental measurement of the optical spectrum of P2-PDWs (green solid line) and corresponding numerical simulations (purple line).

7. Writing operation of P2-PDWs

To demonstrate the potential of these P2-PDWs for all-optical data storage applications, we have evaluated their capacity and robustness against specific manipulations (writing and temporal tweezing) by means of engineered phase perturbations applied to the driving beam. To this aim, we first describe the writing operation of a particular sequence of P2-PDWs corresponding to the 5-bit ASCII code of the acronym "DW": 0010010111. The resonator is first prepared in its symmetry broken HSSs by setting the phase detuning value to $\delta_0 = 1.16$ rad and driving power to 11 W. Meanwhile, the 10-GHz shallow phase modulation is continuously applied on the driving beam to provide a temporal reference grid for this all-optical buffer. Subsequently, a synchronized phase-encoded "DW" kick-perturbation, corresponding to a bit-sequence of localized phase-shifts of $\pi/2$ applied over 500 consecutive round-trips, is locally added on the driving beam to excite the P2-PDWs sequence along the corresponding bit-slots. Figures 6(a-b) summarize the whole writing operation as a function of laboratory time for both polarization components. At the starting point of the experiment

(0 sec), the cavity is well initialized in its symmetry broken HSSs — all the energy is mostly contained in the E_+ hybrid mode. Subsequently, the writing process takes place just beyond 10 sec, with the accurate emergence of the "DW" P2-PDWs pattern. In similar fashion to Figs. 3(c-d), we can notice the perfect anti-correlation between both polarization components, meaning that the P2-PDWs are efficiently generated. The data sequence then propagates along the fiber ring for additional 30 sec, corresponding to millions of cavity photon life-times. Finally, the shallow phase modulation is turned off after 40 sec to reset the optical buffer in virtue of the natural desynchronization of the driving pulse train with respect to the cavity FSR. Note that consecutive writing/erasing operations have been also successfully performed (not shown here) following the same procedure and that the erasing or more generally a modification of the pattern can be achieved through an additional phase perturbation applied on the holding beam. This proof-of-principle experiment confirms the ability of P2-PDWs to be addressed individually as bit-entities in an all-optical buffer.

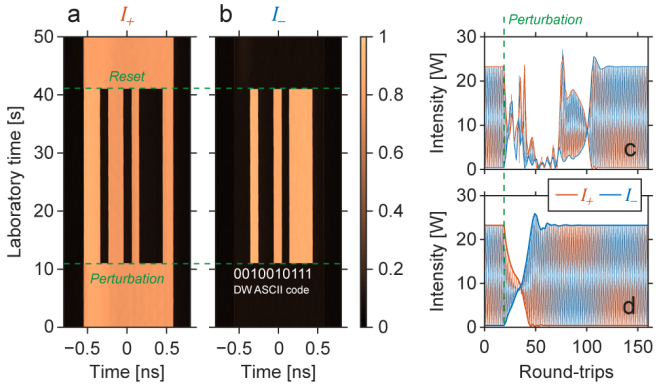

Fig. 6. (a-b) Experimental evolution of polarization components I_+ and I_- with respect to laboratory time recorded during the writing operation of a P2-PDWs sequence. Only even round-trips are reported. (c) Numerical simulations of writing process based on phase perturbation. The graph displays the power of both polarization components as a function of consecutive round-trips. For clarity, the power of each component is also reported on even round-trips with red and blue solid lines. The green dashed-line indicates the local perturbation. (d) Same as panel (c) but for polarization-based writing operation.

However, it is important to stress that the phase perturbation method involved in this experiment is not 100% efficient, and can lead to the emergence of additional and inaccurate P2-PDWs structures in the final data sequence. To further address this point, we have compared numerically in Figs. 6(c-d) two methods of switching operation based respectively, on phase- and polarization-perturbations. Figure 6(c) depicts the power evolution of both polarization components when a localized $\pi/2$-phase perturbation is applied on the driving field over 20 consecutive round-trips (green vertical dashed-line). We first notice the swapping P2 dynamics occurring at every cavity round-trip. Therefore, for sake of clarity, we have also highlighted the power evolution of both polarization components on even round-trips (red and blue solid lines). Just beyond the phase perturbation, a transient regime takes place during nearly 100 of round-trips before the final switching of both polarization components occurs with the emergence of a new anti-phase stationary regime. We can thus presume that this transient behavior, sometimes erratic, as well as potential interactions with neighboring bits, could eventually lead to erroneous writing operations. Note that applying this phase perturbation every second round-trip (synchronized on the P2 periodicity) does not provide better performances. A more reliable technique can however be exploited based on specific polarization perturbations. Figure 6(d) illustrates such a scenario in which a localized polarization perturbation is applied on the driving beam along 20 consecutive round-trips. This perturbation consists of a local change of ellipticity ($\delta_\chi \simeq \pi/4$) in the driving beam leading to a strong depression along the I_+ component i.e., a rise of intensity along the I_- mode. It is also important to note that this perturbation has to be applied on a two-round-trip cycle to efficiently modify the two polarization components in phase with the P2 dynamics. We can then observe the efficient polarization switching of both components with almost no transient regime. These numerical results demonstrate the potential of polarization-based perturbations for efficient P2-PDW writing operations but the experimental realization remains beyond the scope of this paper.

8. Temporal tweezing of P2-PDWs

The second series of experiments deal with the temporal manipulations of P2-PDWs. For this purpose, we exploit an electrical phase shifter, driven by an AWG to dynamically reconfigure the temporal-grid imposed by the 10-GHz shallow phase modulation. More precisely, as in retiming functionalities and CSs buffering experiments [31-33], the PDWs are here forced to follow the spatio-temporal motion imposed by the gradient of this modulation and change their location according to the local minima of the phase profile. Note that this temporal trapping location is the opposite of that observed for bright CSs which, operating in anomalous dispersion regime, are respectively trapped to the peak of the phase modulation.

For this proof-of-principle, we first write a dual bright/dark vectorial structure composed of two P2-PDWs thanks to a 100-ps localized phase perturbation imprinted on the driving field. After a short transient regime, a 100-ps polarization domain emerges in the center of the ns-pulse, trapped to the 10-GHz temporal-grid. Figure 7(a) depicts the temporal profile of this resulting vectorial entity. A bright pulse is generated along the I_+ component (red solid line), and appears enclosed within a dark localized structure in the I_- component (blue solid line), forming a short and well-confined polarization domain. As expected, the total intensity in green, still remains nearly constant.

Figures 7(b-d) illustrate a typical spatio-temporal manipulation of P2-PDWs as a function of laboratory time. For these measurements, the phase-shifter imposes a snaking motion at a frequency close to 1 kHz and a displacement amplitude of 200 ps. We can clearly observe the efficient temporal tweezing of these P2-PDWs without major impairments. Indeed, the two polarization components [panels (b-c)] exactly follow the slow-time trajectory imposed by the phase-shifter, remaining perfectly synchronized and anticorrelated. Moreover, the total intensity [panel (d)] does not reveal any sign of this temporal manipulation, thus confirming that this motion stems from a pure polarization dynamic.

To go beyond this basic proof-of-principle, we have next programmed more complex trajectories into the AWG. Two examples are reported in Figs. 7(e) and 7(f) in a form of "mum" and "bright soliton" motions. For clarity, only the bright structure, corresponding to the polarization component I_+ is displayed. As in the previous results, the P2-PDWs appear perfectly trapped by the phase modulation and strictly follow the trajectory imposed by the phase potential. These different temporal manipulations further demonstrate the robustness and the potential of these new vectorial dissipative solitons for all-optical data storage applications.

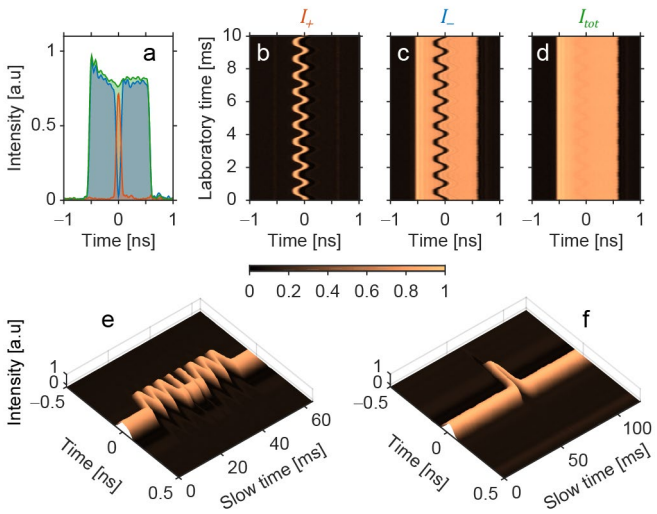

Fig. 7. (a) Intensity profile of the P2-PDWs involved in the temporal tweezing experiment, $\delta_0 = 1.16$ rad and the driving power is 11 W. The two polarization components I_+ and I_- are depicted in red and blue, the total intensity in green. (b-d) Spatio-temporal diagrams showing the evolution of the temporal profile of the P2-PDWs as a function of laboratory time when a sinusoidal snaking motion is applied onto the 10-GHz shallow phase modulation. (b) I_+ component displayed on even round-trips. (c) I_- component. (d) Total intensity. (e) Space-time-intensity diagram reporting the evolution of the I_+ component on even round-trips when a "mum"-shaped temporal trajectory is applied onto the 10-GHz shallow phase modulation. (f) Same as panel (e) for a "bright soliton"-shaped temporal motion.

9. Conclusion

In conclusion, we have reported on the experimental demonstration of temporal manipulations of period-2 dissipative polarization domain wall solitons (P2-PDWs) stored in a normally dispersive fiber Kerr resonator. These localized structures originate from the polarization instability of the scalar homogeneous steady state due to a spontaneous symmetry breaking mechanism mediated by the nonreciprocity of cross-phase modulation occurring between two hybrid eigenmodes of opposite handedness. Moreover, these vectorial entities benefit from a self-protection against system's asymmetries by virtue of a precessing motion imposed by a π-phase shift birefringent defect inserted directly into the cavity, which makes the two polarization components to swap at every cavity round-trip.

The excitation and persistence of P2-PDW patterns have been experimentally evidenced in a 12-m long fiber ring cavity with ultra-long storage performances, obtained without any specific precautions, thus evidencing the key role played by the P2 averaging dynamics. Thanks to engineered phase-perturbations, we also showed that these P2-PDWs can be individually addressed and temporally manipulated as bit-entities in proof-of-concept buffering experiments. Our results confirm that dissipative localized structures circulating within Kerr resonators are promising candidates for the development of stable all-optical memories. More generally, this work provides fundamental insights into the exploitation of ultra-robust spontaneous symmetry breaking phenomena for practical applications, such as random number generation [46-48], optical data storage [34, 49], all-optical logic gates [50] as well as coherent Ising or Potts machines [51-53]. Finally, our work points the way to new original studies dealing with the design of non-homogenous Kerr resonators and complex manipulations of the intra-cavity field [54-62].

Funding. We acknowledge the CNRS, International Research Project WALL-IN, the Conseil Régional de Bourgogne Franche-Comté, the FEDER-FSE Bourgogne 2014/2020 programs as well as the Royal Society of New Zealand, Marsden Funding (18-UOA-310).

Acknowledgements. We acknowledge Dr B. Garbin and Prof G.-L. Oppo for fruitful discussions.

Disclosures. The authors declare no conflicts of interest.

References

1. A. M. Kosevich, "Dynamical and topological solitons in ferromagnets and antiferromagnets," In Solitons (Elsevier, 1986).
2. D. Y. Parpia, B. K. Tanner, and D. G. Lord, "Direct optical observation of ferromagnetic domains," Nature **303**, 684–685 (1983).
3. D. A. Allwood, G. Xiong, C. C. Faulkner, D. Atkinson, D. Petitand, and R. P. Cowburn, "Magnetic domain-wall logic," Science **309**, 1688–1692 (2005).
4. J.-P. Tetienne *et al.* "The nature of domain walls in ultrathin ferromagnets revealed by scanning nanomagnetometry," Nat. Commun. **6**:6733 (2015).
5. J. A. Currivan-Incorvia, S. Siddiqui, S. Dutta, E. R. Evarts, J. Zhang, D. Bono, C. A. Ross, and M. A. Baldo, "Logic circuit prototypes for three-terminal magnetic tunnel junctions with mobile domain walls," Nat. Commun. **7**:10275 (2016).
6. S. Coen and M. Haelterman, "Domain Wall Solitons in Binary Mixtures of Bose-Einstein Condensates," Phys. Rev. Lett. **87**, 140401 (2001).
7. D.M. Stamper-Kurn and M. Ueda, "Spinor Bose gases: Symmetries, magnetism, and quantum dynamics," Rev. Mod. Phys. **85**, 1191 (2013).
8. F. Tsitoura, U. Gietz, A. Chabchoub, and N. Hoffmann, "Phase Domain Walls in Weakly Nonlinear Deep Water Surface Gravity Waves," Phys. Rev. Lett. **120**, 224102 (2018).
9. V. E. Zakharov and A. V. Mikhailov, "Polarization domains in nonlinear optics," JETP Lett. **45**, 349 (1987).
10. M. Haelterman and A. P. Sheppard, "Polarization domain walls in diffractive or dispersive Kerr media," Opt. Lett. **19**, 96–98 (1994).
11. M. Haelterman and A. P. Sheppard, "Vector soliton associated with polarization modulational instability in the normal-dispersion regime," Phys. Rev E **49**, 3389–3399 (1994).
12. B. A. Malomed, "Optical domain walls," Phys. Rev. E 50, 1565-1571 (1994).

13. A. L. Berkhoer and V. E. Zakharov, "Self-excitation of waves with different polarizations in nonlinear media," Sov. Phys. JETP **31**, 486–490 (1970).
14. P. Kockaert, M. Haelterman, S. Pitois, and G. Millot, "Isotropic polarization modulational instability and domain walls in spun fibers," Appl. Phys. Lett. **75**, 2873–2875 (1999).
15. H. Zhang, M. Gilles, M. Guasoni, B. Kibler, A. Picozzi, and J. Fatome, "Isotropic polarization modulational instability in single-mode conventional telecom fibers," J. Opt. Soc. Am. B **36**, 2445–2451 (2019).
16. M. Gilles, P.-Y. Bony, J. Garnier, A. Picozzi, M. Guasoni, and J. Fatome, "Polarization domain walls in optical fibres as topological bits for data transmission," Nat. Photon. **11**, 102–107 (2017).
17. L. W. Quinton and R. Roy, "Fast polarization dynamics of an erbium-doped fiber ring laser," Opt. Lett. **21**, 1478–1480 (1996).
18. H. Zhang, D. Y. Tang, L. M. Zhao, and X. Wu, "Observation of polarization domain wall solitons in weakly birefringent cavity fiber lasers," Phys. Rev. B **80**, 052302 (2009).
19. C. Lecaplain, P. Grelu, and S. Wabnitz, "Polarization-domain-wall complexes in fiber lasers," J. Opt. Soc. Am. B **30**, 211–218 (2013).
20. M. Marconi, J. Javaloyes, S. Barland, S. Balle, and M. Giudici, "Vectorial dissipative solitons in vertical-cavity surface-emitting lasers with delays," Nat. Photon **9**, 450–455 (2015).
21. J. Fatome, B. Kibler, F. Leo, A. Bendahmane, G.-L. Oppo, B. Garbin, S. G. Murdoch, M. Erkintalo, and S. Coen, "Polarization modulation instability in a nonlinear fiber Kerr resonator," Opt. Lett. **45**, 5069–5072 (2020).
22. B. Garbin, J. Fatome, G.-L. Oppo, M. Erkintalo, S. G. Murdoch, and S. Coen, "Dissipative polarization domain walls in a passive driven Kerr resonator," Phys. Rev. Lett. **126**, 023904 (2021).
23. M. Haelterman, S. Trillo, and S. Wabnitz, "Polarization multistability and instability in a nonlinear dispersive ring cavity," J. Opt. Soc. Am. B **11,** 446–456 (1994).
24. B. Garbin, J. Fatome, G.-L. Oppo, M. Erkintalo, S. G. Murdoch, and S. Coen, "Asymmetric Balance in Symmetry Breaking," Phys. Rev. Research **2**, 023244 (2020).
25. N. Moroney, L. Del'Bino, S. Zhang, M. T. M. Woodley, L. Hill, T. Wildi, V. J. Wittwer, T. Südmeyer, G.-L. Oppo, M. R. Vanner, V. Brasch, T. Herr, and P. Del'Haye, "A Kerr Polarization Controller," Nat Commun **13**, 398 (2022).
26. L. Del Bino, J. M. Silver, M. T. Woodley, S. L. Stebbings, X. Zhao, and P. Del'Haye, "Microresonator isolators and circulators based on the intrinsic nonreciprocity of the Kerr effect," Optica **5**, 279–282 (2018).
27. L. Hill, G.-L. Oppo, M. T.Woodley, and P. Del'Haye, "Effects of self-and cross-phase modulation on the spontaneous symmetry breaking of light in ring resonators," Phys. Rev. A **101**, 013823 (2020).
28. A. E. Kaplan and P. Meystre, "Enhancement of the Sagnac effect due to nonlinearly induced nonreciprocity," Opt. Lett. **6**, 590–592 (1981).
29. L. Del Bino, J. M. Silver, S. L. Stebbings, and P. Del'Haye, "Symmetry breaking of counter-propagating light in a nonlinear resonator," Sci. Rep. **7**, 43142 (2017).
30. S. Coen, B. Garbin, G. Xu, L. Quinn, N. Goldman, G.-L. Oppo, M. Erkintalo, S. G. Murdoch, and J. Fatome, "Nonlinear topological symmetry protection in a dissipative system," arXiv:2303.16197 (2023).
31. J. K. Jang, M. Erkintalo, S. Coen, and S. G. Murdoch, "Temporal tweezing of light through the trapping and manipulation of temporal cavity solitons," Nat. Commun. **6**, 7370 (2015).
32. B. Garbin, J. Javaloyes, G. Tissoni, and S. Barland, "Topological solitons as addressable phase bits in a driven laser," Nat Commun **6**, 5915 (2015).
33. J. K. Jang, M. Erkintalo, J. Schröder, B. J. Eggleton, S. G. Murdoch, and S. Coen, "All-optical buffer based on temporal cavity solitons operating at 10 Gb/s," Opt. Lett. **41**, 4526–4529 (2016).
34. G. Xu, A. Nielsen, B. Garbin, L. Hill, G.-L. Oppo, J. Fatome, S. G. Murdoch, S. Coen and M. Erkintalo, "Spontaneous symmetry breaking of dissipative optical solitons in a two-component Kerr resonator," Nat. Commun. **12**, 4023 (2021).
35. Z. Lu, H. J. Chen, W. Wang et al. "Synthetized soliton crystals," Nat. Commun. **12**, 3179 (2021).
36. S. Barland, S. Coen, M. Erkintalo, M. Giudici, J. Javaloyes, and S. G. Murdoch, "Temporal localized structures in optical resonators," Advances in Physics: X **2:3**, 496–517 (2017).
37. R. Vallée, "Temporal instabilities in the output of an all-fiber ring cavity," Opt. Commun. **81**, 419–426 (1991).
38. M. Haeltermann, S. Trillo, and S. Wabnitz, "Dissipative modulation instability in a nonlinear dispersive ring cavity," Opt. Commun. **91,** 401–407 (1992).
39. S. Wabnitz, "Suppression of soliton interactions by phase modulation," Electron. Lett. **29**, 1711–1713 (1993).
40. N. J. Smith, W. J. Firth, K. J. Blow, and K. Smith, "Suppression of soliton interactions by periodic phase modulation," Opt. Lett. **19**, 16–18 (1994).
41. A. Jiang, M. E. Grein, H. A. Haus, E. P. Ippen, and H. Yokoyama, "Timing jitter eater for optical pulse trains," Opt. Lett. **28**, 78–80 (2003).
42. G. P. Agrawal, Nonlinear Fiber Optics (5th ed., Academic Press, Oxford, 2013).
43. M. Liu, D. A. Powell, I. V. Shadrivov, M. Lapine, and Y. S. Kivshar, "Spontaneous chiral symmetry breaking in metamaterials," Nat Commun **5**, 4441 (2014).
44. Di Che, An Li, Xi Chen, Qian Hu, Yifei Wang, and William Shieh, "Stokes vector direct detection for short-reach optical communication," Opt. Lett. **39**, 3110–3113 (2014).
45. S. Malaguti, M. Conforti, and S. Trillo, "Dispersive radiation induced by shock waves in passive resonators," Opt. Lett. **39**, 5626–5629 (2014).
46. Y. Okawachi, M. Yu, K. Luke, D. O. Carvalho, M. Lipson, and A. L. Gaeta, "Quantum random number generator using a microresonator-based Kerr oscillator," Opt. Lett. **41**, 4194–4197 (2016).
47. T. Steinle, J. N. Greiner, J. Wrachtrup, H. Giessen, and I. Gerhardt, "Unbiased All-Optical Random-Number Generator," Phys. Rev. X **7**, 041050 (2017).
48. L. Quinn, G. Xu, Y. Xu, Z. Li, J. Fatome, S. G. Murdoch, S. Coen, and M. Erkintalo, "Random number generation using spontaneous symmetry breaking in a Kerr resonator," arXiv:2305.07155 (2023).
49. L. Del Bino, N. Moroney, and P. Del'Haye, "Optical memories and switching dynamics of counterpropagating light states in microresonators," Opt. Express **29**, 2193–2203 (2021).
50. N. Moroney, L. Del Bino, M. T. M. Woodley, G. N. Ghalanos, J. M. Silver, A. Ø Svela, S. Zhang, and P. Del'Haye, "Logic Gates Based on Interaction of Counterpropagating Light in Microresonators," J. Lightwave Technol. **38**, 1414–1419 (2020).
51. T. Inagaki *et al.,* "A coherent Ising machine for 2000-node optimization problems," Science **354**, 603–606 (2016).
52. T. Honjo *et al.,* "100,000-spin coherent Ising machine," Sci. Adv. **7**, eabh0952 (2021).
53. M. Honari-Latifpour, and M.-A. Miri, "Optical Potts machine through networks of three-photon down-conversion oscillators," Nanophotonics **9**, 4199–4205 (2020).
54. N. Englebert, F. De Lucia, P. Parra-Rivas, C. Mas Arabi, P.-J. Sazio, S.-P. Gorza, and F. Leo, "Parametrically driven Kerr cavity solitons," Nat. Photon. **15**, 857–861 (2021).
55. F. Bessin, A. M. Perego, K. Staliunas, S. K. Turitsyn, A. Kudlinski, M. Conforti, and A. Mussot, "Gain-through-filtering enables tuneable frequency comb generation in passive optical resonators," Nat Commun. **10**, 4489 (2019).
56. C. Spiess, Q. Yang, X. Dong, V. G. Bucklew, and W. H. Renninger, "Chirped dissipative solitons in driven optical resonators," Optica **8**, 861–869 (2021)
57. A. Tikan, A. Tusnin, J. Riemensberger, M. Churaev, K. Komagata, X. Ji, R. N. Wang, J. Liu, and T. J. Kippenberg, "Protected generation of dissipative Kerr solitons in supermodes of coupled optical microresonators," Sci. Adv. **8**, eabm6982 (2022).
58. S.-P. Yu, E. Lucas, J. Zang, and S. B. Papp, "A continuum of bright and dark pulse states in a photonic-crystal resonator," Nat. Commun. **13**, 3134 (2022).

59. Wang *et al.,* "Experimental observation of Berry phases in optical Möbius-strip microcavities," Nat. Photon. **17**, 120–125 (2023).
60. K. Tusnin, A. M. Tikan, and T. J. Kippenberg, "Nonlinear states and dynamics in a synthetic frequency dimension," Phys. Rev. A **102**, 023518 (2020).
61. N. Englebert, N. Goldman, M. Erkintalo, N. Mostaan, S.-P. Gorza, F. Leo, and J. Fatome, "Bloch oscillations of driven dissipative solitons in a synthetic dimension," Nat. Phys. (2023).
62. L. Yuan, A. Dutt, and S. Fan, "Synthetic frequency dimensions in dynamically modulated ring resonators," APL Photonic **6**, 071102 (2021).